Article

Electrochemical Detection of a Few Copies of Unamplified SARS-CoV-2 Nucleic Acids by a Self-Actuated Molecular System

Daizong Ji, Mingquan Guo, Yungen Wu, Wentao Liu, Shi Luo, Xuejun Wang, Hua Kang, Yiheng Chen, Changhao Dai, Derong Kong, Hongwenjie Ma, Yunqi Liu, and Dacheng Wei*

Read Online

ACCESS | Metrics & More | Article Recommendations | Supporting Information

ABSTRACT: The existing electrochemical biosensors lack controllable and intelligent merit to modulate the sensing process upon external stimulus, leading to challenges in analyzing a few copies of biomarkers in unamplified samples. Here, we present a self-actuated molecular-electrochemical system that consists of a tentacle and a trunk modification on a graphene microelectrode. The tentacle that contains a probe and an electrochemical label keeps an upright orientation, which increases recognition efficiency while decreasing the pseudosignal. Once the nucleic acids are recognized, the tentacles nearby along with the labels are spontaneously actuated downward, generating electrochemical responses under square wave voltammetry. Thus, it detects unamplified SARS-CoV-2 RNAs within 1 min down to 4 copies in 80 μL, 2–6 orders of magnitude lower than those of other electrochemical assays. Double-blind testing and 10-in-1 pooled testing of nasopharyngeal samples yield high overall agreement with reverse transcription-polymerase chain reaction results. We fabricate a portable prototype based on this system, showing great potential for future applications.
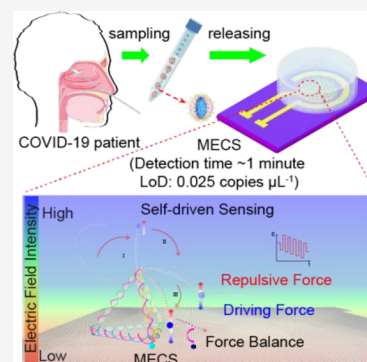
INTRODUCTION

The severe acute respiratory syndrome coronavirus 2 (SARS-CoV-2) causing coronavirus disease 2019 (COVID-19) has infected over 515 million people including 6,255,965 deaths through the middle of 2022. Multiple variants have emerged, such as Beta, Delta, and Omicron.[1–4] Nucleic acid testing by a reverse transcription-polymerase chain reaction (RT-PCR) is acknowledged as the golden standard to diagnose COVID-19 as well as other infectious diseases such as Zika and Ebola.[5–8] However, it requires time-consuming nucleic acid extraction and amplification processes performed in specialized laboratories.[9–14] To curb the virus outspreading, it is necessary to simplify the testing procedure while guaranteeing accuracy.[8,15–18] Until now, various technologies have been developed to solve the above issues. Among these technologies, electrochemical biosensing, especially electrochemical biosensing based on microelectrodes, has been widely studied because of its rapid response, high current density, simple operation, low cost, and portability.[19,20] These advantages make the electrochemical biosensor a great candidate for nucleic acid testing.[21–24]

The electrochemical sensors face a long-standing challenge to ultrasensitively detect biomarkers at a level of several copies.[25–27] It is attributed to the uncontrollability in the sensing operation as follows. First, the missing acting force orients the probes upward making the probes prone to entangle or adsorb to the electrode surface, which inactivates the probes and decreases the biorecognition efficiency. Second, there exist possibilities that the electrochemical labels move

close to the electrode, leading to pseudosignal and low accuracy when detecting trace nucleic acids. Third, the sensing process lacks spontaneity upon biorecognition; thus, the signal transduction has low efficiency and the signals are easily drowned out by the background noises.[19,28] At present, due to their insufficient sensitivity, nucleic acid testing by electrochemistry relies on amplification of genetic species. After amplification, the limit of detection (LoD) is 10^{-15}–10^{-18} M, approximately 60–60000 copies in 80 μL of testing solution.[29–32] When testing unamplified SARS-CoV-2 RNAs, the lowest LoD is only 147 to 552 copies in 80 μL of testing solution.[33–35]

Organisms on the earth have undergone a long-term evolutionary process, which has thus been the source of all kinds of technical ideas, engineering principles, and great inventions.[36–41] Hydras can keep their tentacles upright afloat voluntarily, featuring efficient responses and accurate self-motion when recognizing external stimuli.[42–44] Here, we demonstrate a self-actuated molecular-electrochemical system (MECS) modified on a graphene microelectrode. MECS consists of a tentacle and a trunk constructed by DNA nanostructure. The probe and electrochemical label on the
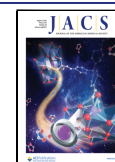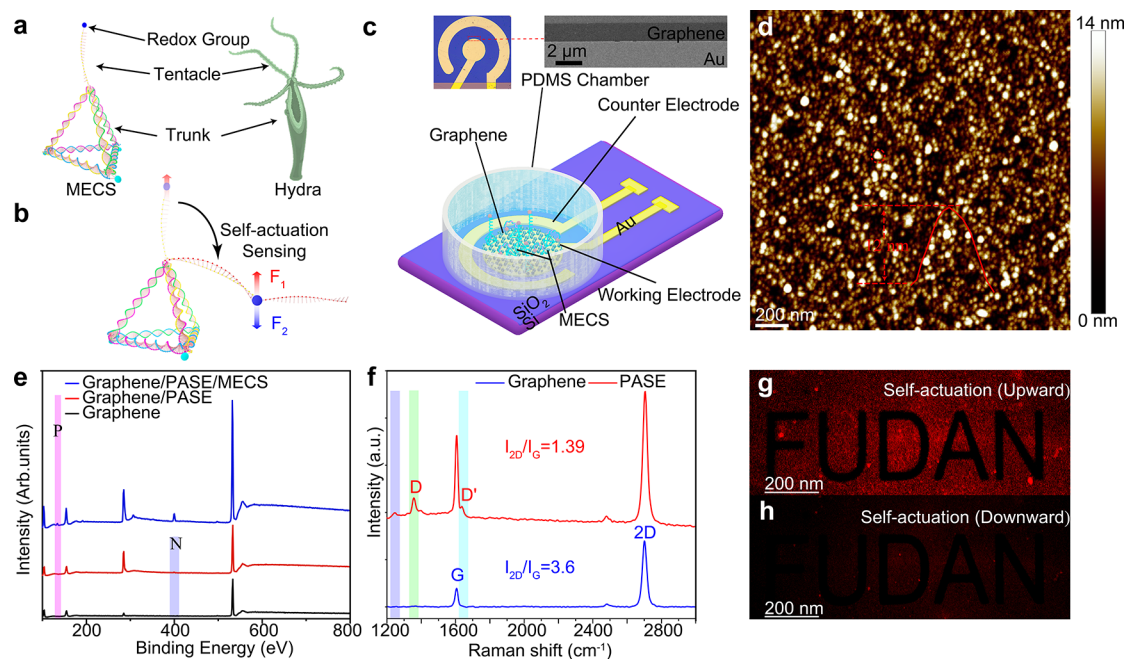
Figure 1. MECS and MECS-modified graphene microelectrode. (a) Structure of the proposed MECS based on DNA nanostructures that mimic the hydra architecture. (b) Schematic illustration of MECS for the RNA sensing process; F1 represents the upward repulsion force of the local electric field that pulls the tentacle away from the electrode, and F2 represents the downward driving forces and steric effects that actuate the tentacle close to the electrode. (c) Device configuration of the MECS-modified graphene microelectrode (inset: optical microscope image of the working electrode and SEM image of graphene). (d) AFM image of the graphene modified with MECS in fluids. (e) XPS survey data of pristine, PASE-treated graphene, and MECS/PASE-modified graphene. (f) Representative Raman spectra of pristine graphene (red line) and PASE-treated graphene (blue line). Fluorescence intensity images of the graphene immobilized with MECS before (g) and after (h) addition of SARS-CoV-2 IVT RNA, respectively.

tentacle maintain an upright orientation, which improves biorecognition and avoids pseudosignal. After recognizing targeted nucleic acids, the configuration of the tentacles nearby changes spontaneously, pushing the electrochemical labels downward. The configuration change can be further modulated by electrical excitations of square wave voltammetry (SWV) or differential pulse voltammetry (DPV). Owing to the self-actuated sensing process at the molecular scale, MECSs overcome the aforementioned limitations, enabling electrochemical detection of SARS-CoV-2 in vitro transcribed (IVT) RNA down to ~80 zM (1 zM = 10^{-21} M), equivalent to four copies in 80 μL of saliva. Without nucleic acid amplification, double-blind testing and 10-in-1 pooled testing of clinical samples are performed within 1 min and exhibit high consistency with RT-PCR results. Finally, a portable MECS-based prototype is developed for point-of-care SARS-CoV-2 testing.

■ RESULTS AND DISCUSSION

MECS and MECS-Modified Graphene Microelectrodes. As shown in Figure 1a, the hydra consists of a tentacle and an upstanding trunk. Inspired by the hydra, the trunk of MECS as a prop unit is a regular tetrahedral structure with four double-stranded DNAs (ds-DNA) that intertwine to form edges. A flexible single-stranded DNA (ss-DNA) extends from the top vertex of the tetrahedral trunk as the tentacle. The tentacle contains a probe targeting ORF1ab genes of SARS-CoV-2 RNA as a recognition unit, 5 thymine nucleotides as swivel bearing for free-movement of tentacle after target recognition, and an electrochemical label of methylene blue as signal generator at the tip of tentacle (Table S1). In the testing,

a negative potential was applied on the graphene microelectrode. Owing to negative charges on the ss-DNA backbones, the tentacle remains upright spontaneously in the local electrical field on the graphene surface (Figure 1b). Once nucleic acids are recognized, the steric effect as well as the electrostatic force generated by the negative charges of the targets actuate the tentacle downward to the electrode surface automatically. The bottom of the trunk carries the amino groups to imitate the basal disk, which are used as a modification unit to link to 1-pyrenebutanoic acid succinimidyl ester (PASE) on the working electrode of graphene electrode (Figure 1c and Figures S1 and S2). Finally, a polydimethylsiloxane (PDMS) chamber is attached to the electrodes to hold the testing solution.

As shown in an atomic force microscope (AFM) image measured in fluids, MECSs maintain their three-dimensional structures and are uniformly anchored on the graphene surface (Figure 1d). The theoretic height of a trunk is around 5.3 nm, which approximates the theoretic length of the tentacle (6.8 nm). MECS consists of a tentacle and a trunk with a height around 12 nm in AFM, which is similar to the designed structure. X-ray photoelectron spectroscopy (XPS) and Raman spectra also confirm that the graphene was functionalized with PASE and modified with MECS. Figure 1e and Figure S3a show the XPS of the pristine graphene, PASE-treated graphene, and MECS-modified graphene. The pristine graphene shows no prominent N peak, while the N 1s is observed after PASE treatment. The increased intensity of the P 2p peak indicates that the MECS is successfully modified on the surface of PASE-treated graphene.[45,46] As shown in Figure 1f, Figure S3b, and Figure S3c, the Raman spectra of the
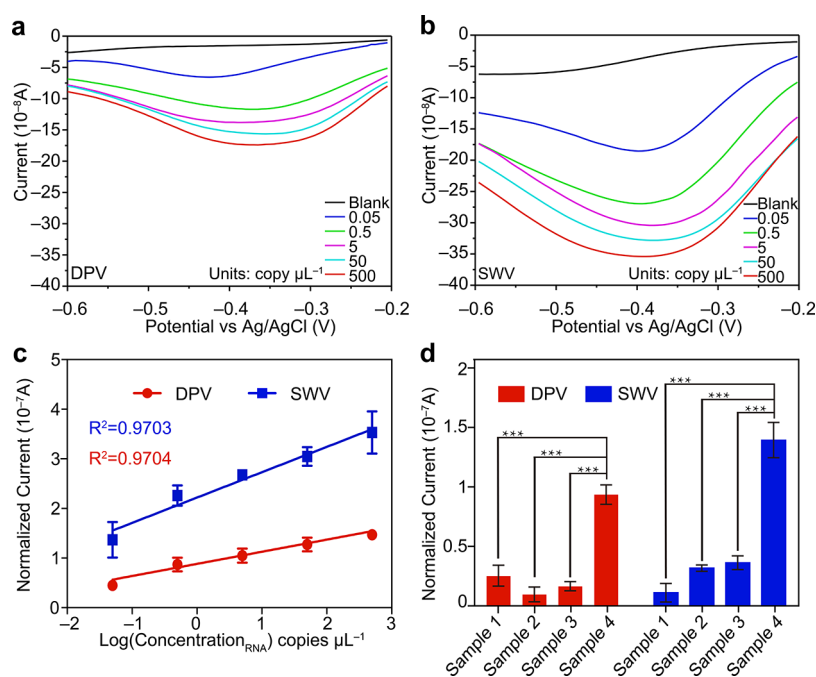
Figure 2. Ultrasensitive electrochemical detection of SARS-CoV-2 IVT RNA using MECS. (a) DPV and (b) SWV response of MECS-modified graphene microelectrode upon addition of SARS-CoV-2 IVT RNA (from 0.05 copies μL^{-1} to 500 copies μL^{-1}) in artificial saliva. (c) Normalized current of DPV (red line) and SWV (blue line) at different concentrations of SARS-CoV-2 IVT RNA in logarithm scale, and error bars represent the standard deviations ($n = 3$). (d) Statistic for specific testing of SARS-CoV-2 RNA, and error bars represent the standard deviations ($n = 3$). The concentrations of sample 1 (human ssDNA), sample 2 (MERS-CoV IVT RNA), and sample 3 (SARS-CoV IVT RNA) are all fixed on 5 copies μL^{-1}, while the concentration of sample 4 (SARS-CoV-2 IVT RNA) is 0.5 copies μL^{-1}.

pristine graphene and PASE-treated graphene surfaces show two prominent peaks (the G and 2D peaks). After PASE treatment, the D peak and D′ peak obviously appeared due to the relative resonance of sp^3 bonding, orbital hybridization, and pyrene group binding on the surface of pristine graphene.[47] After PASE treatment, the average roughness of graphene obtained by AFM increases from 0.231 to 0.483 nm (Figure S4).

Cyclic voltammetry (CV, Figure S5) is performed by using graphene microelectrodes with different modifications. The pristine graphene microelectrode has a peak current of 8.87×10^{-7} A, which is more significant than others. This result indicates the successful modification of MECSs and a dominant edge effect on the microelectrode. To examine the spatial configuration change of the tentacle after capturing SARS-CoV-2 IVT RNA, a fluorescent dye cyanine3 (Cy3), instead of methylene blue, is conjugated at the top of the tentacle. When 10^8 copies of SARS-CoV-2 IVT RNA are added in the PDMS chamber, Cy3 fluorescence quenches (Figure 1g,h). The results indicate that the probe and the electrochemical label remain upward on the trunk. Capturing the SARS-CoV-2 RNA arouses the tentacle together with Cy3 close to the graphene surface.

Detection of SARS-CoV-2 IVT RNA. The performance of MECS-modified graphene microelectrode is investigated by detecting SARS-CoV-2 RNA using DPV and SWV. Before detection, the incubation time is optimized by measuring the electrochemical current response every 5 min using SWV and DPV, respectively. As shown in Figure S6, the electrochemical current response of both SWV and DPV is almost constant after 25−30 min. Hence, SARS-CoV-2 RNA detection is determined 30 min after sample addition. We studied the stability of the baseline over time and over operation. The

addition and removal processes of the blank sample do not lead to an electrochemical signal, indicating the stability of the baseline over operation and over time (Figure S7). After the SARS-CoV-2 RNA sample is added, the redox current as the electrochemical response appears in the DPV and SWV curves. Over the next 30 min, the electrochemical response also remains almost unchanged. The results show that SARS-CoV-2 RNA leads to an electrochemical response, not the disturbance of the adding sample procedure. As shown in Figure 2a,b, the concentration of SARS-CoV-2 IVT RNA increased from 0.05 to 500 copies μL^{-1}, while the peak current of electrochemical response enhanced to approximately 3.5×10^{-7} A and 1.8×10^{-7} A using SWV and DPV, respectively. The testing is repeated three times to investigate the relationship between the concentration of SARS-CoV-2 IVT RNA and normalized electrochemical current of DPV and SWV. The normalized current signal yielded by both SWV and DPV is plotted as a function of SARS-CoV-2 RNA concentration on a logarithm scale in Figure 2c, showing linear correlations that can be described as

$$I_{DPV} = 0.244 \log C_{RNA} + 0.883 \tag{1}$$

$$I_{SWV} = 0.52 \log C_{RNA} + 0.223 \tag{2}$$

where C_{RNA} (copies μL^{-1}) is the concentration of SARS-CoV-2 IVT RNA. I_{SWV} and I_{DPV} (10^{-7} A) represent the normalized electrochemical current response on the sensors measured by SWV and DPV, respectively. The LoD of SARS-CoV-2 IVT RNA testing was estimated as 0.035 and 0.025 copies μL^{-1} for DPV and SWV measurements, respectively, with 3δ/slope calculation using the dose-dependent fitting curve. The results showed that SWV on MECS had higher sensitivity (slope = 0.52) than DPV (slope = 0.244). The relative standard
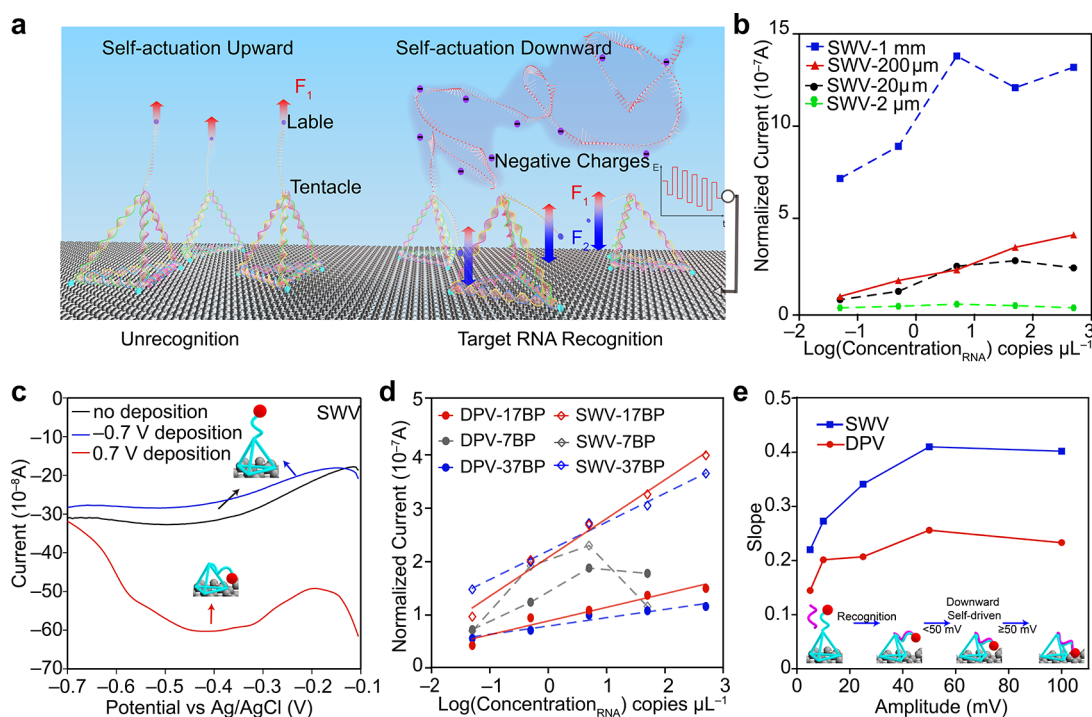
Figure 3. Mechanism of MECS for ultrasensitive detection of SARS-CoV-2 RNA. (a) Schematic diagram of MECS for RNA detection with specific biorecognition and signal transduction in biofluid. F_1 represents the upward repulsion force of the local electric field that pulls the tentacle away from the electrode, and F_2 represents the downward driving forces and steric effect that actuates the tentacle close to the electrode. (b) Normalized current response of electrodes with different radii at different concentration of SARS-CoV-2 IVT RNA using SWV. (c) SWV response of MECS with different voltage deposition (0.7 and −0.7 V) and without deposition in whole artificial saliva. Inset: schematic diagram of MECS under different depositions. (d) Normalized current response of electrodes modified with different trunk heights of MECS using SWV and DPV. (e) Slope of the dose-depend curve at different amplitudes of actuation using DPV and SWV. Inset: schematic diagram of MECS under different amplitudes for detection.

deviation (RSD) can quantify the uniformity of the sensing performances. As shown in Table S2, the RSD of MECS-modified sensor for detecting SARS-CoV-2 RNA by DPV is 11.414%, while that for detecting SARS-CoV-2 RNA by SWV is 4.667%. Thus, the sensors have high uniformity. To demonstrate the testing stability, we repeat DPV and SWV testing every 10 s (Figure S8). All results have no redox current response when testing blank samples, while stable electrochemical signals are obtained when testing the SARS-CoV-2 RNA sample after incubation for 30 min, indicating high testing stability. Figure 2d displayed the specificity of SARS-CoV-2 IVT RNA using MECS-modified graphene microelectrode with both SWV and DPV. The concentrations of MERS IVT RNA, SARS-CoV IVT RNA, and human IVT ssDNA are 5 copies μL^{-1}, while the concentration of SARS-CoV-2 IVT RNA is just 0.5 copies μL^{-1}. As shown in Figure S9, MERS IVT RNA, SARS-CoV IVT RNA, and human IVT ssDNA have no electrochemical current response in both SWV and DPV, only changes in the base current, indicating that the tentacles of MECS capture none of these nucleic acids. In contrast, SARS-CoV-2 IVT RNA with only a tenth of the concentration of these above-mentioned nucleic acids had electrochemical current response in both SWV and DPV. The current responses of SARS-CoV-2 IVT RNA (9.36×10^{-8}A for DPV and 1.39×10^{-7}A for SWV) exceed three times these above-mentioned nucleic acids in repeat testing, showing a statistical difference ($P < 0.001$). The results suggested that MECS had a good specificity toward SARS-CoV-2 RNA without the interference of other nucleic acids. Long-term stability is important for the application. Both DPV and SWV

curves of the blank sample show no redox current, while the redox current occurs and increases with concentration of SARS-CoV-2 RNA (Figure S10). The electrochemical response maintains a certain value after 3 weeks. Thus, MECS-modified sensors maintain high sensitivity after long-term storage.

Sensing Mechanism. Self-actuated biorecognition and signal transduction are keys to the sensitivity of the MECS biosensor. As shown in Figure 3a and Figure S11, inspired by hydra, the tetrahedron trunk of MECS orients upright so as to prevent the aggregation of adjacent tentacles and their nonspecific adsorption to the graphene. Meanwhile, the free tentacle maintains away from the electrode automatically under an electrostatic repulsive force, minimizing a possible pseudosignal. Upon target recognition, the steric effect and the heavily charged nucleic acid cloud result in a significant conformation change of tentacles. Thus, the tentacle as well as nearby labels move downward spontaneously via the repulsive force to the vicinity of the interface. Then due to the modulation of the repulsion force caused by the electric field of SWV or DPV, the tentacle can be controllably actuated closer to an electrode (Figure S12). Such a self-actuated mechanism yields an appreciable electrochemical response. In previous work, we demonstrated graphene field-effect transistors (g-FETs) for rapid COVID-19 diagnosis.[17,18,48,49] In the case of g-FETs, DNA nanostructures with probes are modified on the graphene surface, and the current signal is associated with potential perturbations when charged analytes are recognized by the probes. Here, MECS has a different principle from that of g-FET. The current signal is associated with the electro-
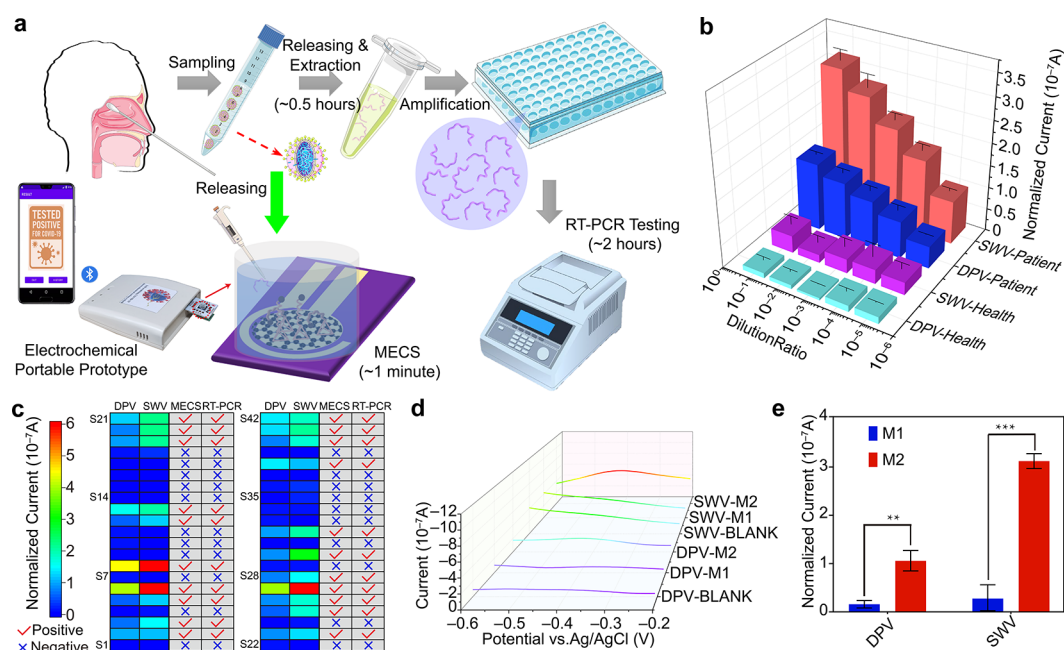
Figure 4. Ultraprecise detection of SARS-CoV-2 RNA clinical samples using MECS. (a) Testing procedures of SARS-CoV-2 clinical samples by RT-PCR- and MECS-modified graphene microelectrode. (b) Statistical data of current responses using DPV and SWV detection for the diluted clinical samples of COVID-19 patients and healthy people; error bars represent the standard deviations ($n = 3$). (c) Current response of clinical samples ($n = 42$) in double-blind testing. (d) Differential pulse voltammogram and square wave voltammogram for pooled samples testing. (e) Statistics of pooled samples tested by DPV and SWV; error bars represent the standard deviations ($n = 3$).

chemical reaction when the labels are actuated downward to the graphene surface. Compared with g-FETs, the MECS-modified sensors have advantages such as simple architecture, high signal readability, and low cost.

Different radii of electrodes are first fabricated to study the edge effect for the sensitive detection and acceptable detection range. The selected electrode radius range was determined by theoretical calculations. The calculation process of the formula is listed in the Supporting Information.

$$\frac{1\partial c}{D\partial t} = \frac{1\partial c}{r\partial r} + \frac{\partial^2 c}{\partial r^2} + \frac{\partial^2 c}{\partial z^2} \tag{3}$$

According to eq 3, the different radii of electrodes are fabricated from 2 μm to 1 mm. As shown in Figure 3b and Figure S13, although the initial current of the 1 mm electrode is largest in all kinds of electrodes, the slope of the 1 mm electrode is smaller than that of the 200 μm electrode. When the concentration of SARS-CoV-2 RNA is larger than 5 copies μL^{-1}, the current does not increase significantly and even decreases. The results indicated that the edge effect does not dominate in the millimeter-scale electrode. Although the electrode with the radius of 20 μm is more sensitive in the first few concentrations, its detection range is much narrower, just from 0.05 to 5 copies μL^{-1}.

The recognized events lead to the tentacle's position and configuration change with the electrochemical group on the graphene electrochemical electrode, which induces electrochemical response changes associated with SARS-CoV-2 RNA in real time. Different deposition voltages for 1 min are applied before DPV and SWV detection (Figure 3c and Figure S14). The tentacles are adsorbed near the electrode surface after 0.7 V deposition to produce an electrochemical response in DPV and SWV, even though there is no target RNA in the artificial saliva. In contrast, there is only a weak electrochemical

responses in the absence of deposition voltage or −0.7 V. The results indicated that under the repulsive force of the negative changed local electric field the tentacle maintains an upright orientation away from the electrode, which is more suitable for target recognition and detection. Then the role of distance regulation between tentacle and electrode for efficient electrochemical signal transduction under modulation of the repulsive force is studied by detecting different concentrations of SARS-CoV-2 RNA using MECS with different trunk heights. The trunk height of 17bp (17bp: 17 base pairs for tetrahedral edges) for the regular tetrahedral structure is around 5.3 nm, approximate to the tentacle length (6.8 nm), while the trunk heights of 7 and 37bp are 2.2 and 11.1 nm, respectively. The 17bp of MECS shows a more comprehensive detection range and higher sensitivity than the 7bp and the 37bp (Figure 3d). Hence, when applying the excitation voltage of SWV and DPV, the change of force balance actuates the tentacle on the trunk of the 17bp regular tetrahedral structure together with the electrochemical group and SARS-CoV-2 RNA downward, being much more controllable and coming closer to the graphene surface than other height of the trunk.

MECS not only simulates the appearance characteristics of hydra to keep the tentacle's activation but also imitates the predation behavior of hydra by controlled force balance of the tentacle to improve signal transduction during SARS-CoV-2 RNA detection. As shown in Figure 3e and Figure S15, different amplitudes imitating the predation behavior of hydra are performed to verify the controlled force balance effects for distance regulation between the tentacle and electrode to enhance the sensitivity. When the amplitude increased from 5 to 50 mV, the slope of the concentration-dependent curve, namely sensitivity, is significantly improved in both DPV and SWV. The slope is almost unchanged when the amplitude is greater than 50 mV. The results indicated that the amplitude of 50 mV can actuate almost all the tentacles that capture the

SARS-CoV-2 RNA to the electrode surface and the redox reaction occurs to generate the signal response. As shown in Figure S16, the excitation voltages of SWV and DPV are used to imitate the different tension of the hydra. The amplitude of SWV is much greater than that of DPV. In summary, the reduction of repulsive force by different electrical fields effects and electrical field forms can control the force balance to regulate the distance between the tentacle and electrode.

Direct Testing of Clinical Samples. Traditional RT-PCR detection requires nucleic acid amplification and purification after RNA extraction (Figure 4a). Here, we simply heat the clinical sample to release RNA. Then the clinical samples are directly detected using a MECS-modified graphene microelectrode. A portable smartphone-based electrochemical system has been developed (Figure S17). It can be used for on-site and point-of-care testing (POCT) outside of laboratories, such as in airports, clinics, local emergency departments, and even at home (Figure S18). We measured the response of the MECS-modified graphene microelectrode to serially diluted clinical samples to estimate the sensing capability for accurate samples. As shown in Figure 4b and Figure S19, an appreciable average current response up to 4.95×10^{-8} and 9.68×10^{-8} A for DPV and SWV, respectively, is observed even with 10^5 dilutions ($\sim$0.04 copies μL^{-1}) in repeat testing, indicating the high sensitivity of MECS. Compared with commercial COVID-19 detection kits and reported diagnosis methodologies, MECS shows the rapid detection time (less than 1 min) and lower LoD (0.025 copies μL^{-1} for SWV and 0.035 copies μL^{-1} for DPV) to SARS-CoV-2 RNA, even in a clinical sample (Table 1).

Then the clinical samples are out of order and tested without nucleic acid amplification using MECS for double-blind testing to verify validity. Although the viral transport medium (VTM) contains a variety of biomolecules, there is no electrochemical signal on MECS in the blank sample (VTM solution) and health sample after 30 min for incubation (Figure S20a,c). The unmistakable electrochemical signal generated after the samples of SARS-CoV-2 patients were added into the PDMS groove and incubated for 30 min (Figure S20b,d). The normalized current responses of SARS-CoV-2 patients' samples are distinctly more significant than those of healthy samples. The results show high overall agreement ($\sim$100%) with the RT-PCR results, which indicates that MECS can be used for the accurate diagnosis of COVID-19 (Figure 4c).

It is well-known that pooled sample testing is one of the most effective methods for large-scale screening to prevent an outbreak of a pandemic. MECS is also employed for 10-in-1 pooled clinical sample testing. Isometric nasopharyngeal swab samples from 10 healthy volunteers' samples were mixed as negative samples (M1), while isometric 9 healthy volunteers' samples and 1 SARS-CoV-2 patient's sample were mixed as positive sample (M2). As shown in Figure 4d, electrochemical currents of 1×10^{-7} and 3×10^{-7} A in SWV and DPV are observed, respectively, in M2, while no redox peak current was observed in M1, which is similar to the blank sample. The statistical data shows that the normalized current of positive pooled samples is larger than that of negative pooled samples, showing a statistical difference ($P < 0.001$) (Figure 4e). The detection times, defined as the electrochemical testing time, for COVID-19 diagnosis are 15 s in SWV and 1 min in DPV, respectively. Hence, the MECS-modified graphene microelectrode could be used for broad COVID-19 screening.

CONCLUSION

In summary, this work demonstrates a MECS constructed by DNA nanostructure for ultrasensitive SARS-CoV-2 RNA testing. The MECS modulates the electrochemical sensing process at molecular scale, solving a challenging issue of electrochemical assay in detection sensitivity. We demonstrate that automatically controlling the position of labels enables the most sensitive electrochemical assay so far for nucleic acid testing.[29−32] The detection of SARS-CoV-2 RNAs approaches the physical limit of 4 copies in 80 μL artificial saliva, 2−6 orders of magnitude lower than other electrochemical biosensors and commercial kits.[33−35] The idea of MECS also has broad application prospects to construct electrochemical biosensors for other infectious diseases like Ebola, Zika, and variants of SARS-CoV-2, such as Beta, Delta, and Omicron, by replacing the nucleotide sequence of the tentacle.

In the application, MECS enables direct testing of unamplified clinical samples. The results of double-blind testing are highly consistent with the RT-PCR results, demonstrating the merit in the ultraprecise diagnoses of COVID-19. More importantly, the MECS can identify positive 10-in-1 pooled clinical samples within 1 min. Pooled testing reduces the cost per test, increases testing efficiency, and has been considered as an effective strategy for population-scale disease screening to alleviate the burden on public healthcare services. Benefiting from the advantages such as rapid detection speed, low cost, and easy operation, MECS sensors hold great promise to solve the current dilemma in SARS-CoV-2 RNA testing and realize worldwide reopening. Combined with smartphone-based electrochemical system, MECS enables on-site and POCT for nucleic acid detection, such as in airports, clinics, local emergency departments, customs and even at home. As we know, antigen testing, mainly gold immunochromatography, is the primary commercial method of COVID-19 home testing.[70,71] However, it can identify only 70% of positive cases.[72] Individuals with low viral load could be ignored. In contrast, benefitting from the self-actuated sensing process at the molecular scale, MECSs overcome the limitations toward monomolecular electrochemical detection, which might be the missing piece of the puzzle enabling electrochemical testing to be a comprehensive tool in future epidemic prevention and control.

METHODS

Fabrication of MECS-Modified Graphene Microelectrodes. The graphene electrochemical microelectrode was fabricated via a thermally assisted bilayer lift-off process based on semiconductor IC processing technology.[73] As shown in Figure S21, fabrication of the graphene electrochemical microelectrode included electrode preparation and graphene transfer. Graphene with poly(methyl methacrylate) (PMMA) transferred from Cu foil by the electrochemical bubbling method was carried out onto the working electrodes. PMMA was subsequently removed by acetone. In electrode preparation, two layers of resist (sacrificial layer LOR 3A and photoresist S1813) were sequentially spin-coated on the SiO_2/Si wafer. The wafer was heat-treated at 170 °C for 5 min and 115 °C for 1 min, respectively. The ultraviolet lithography (Microwriter ML3, Durham Magneto Optics Ltd., UK) was used to pattern the electrode form (working electrode of radius 1 mm, 200 μm, 20 μm, 2 μm). After that, 5/45 nm Cr/Au were deposited on the wafer by using a thermal evaporator

Table 1. Performance Comparison for Commercial COVID-19 Detection Kits, Reported Nucleic Acid Detection Methods, and MECS-Modified Graphene Microelectrode

detection method	disease diagnosis	sample type	target analyte	amplification	LoD	time	ref/company
RT-PCR[a]	COVID-19	Viral RNA	ORF1ab, N, E	Yes	1000 copy mL^{-1}	90 min	Beijing Applied
RT-PCR	COVID-19	Viral RNA	ORF1ab, ORF8	Yes	330 copy mL^{-1}	50 min	BioFire Defense, LLC
RT-PCR	COVID-19	Viral RNA	ORF1ab, S	Yes	500 copy mL^{-1}	1–1.5 h	DiaSorin Molecular LLC
RT-PCR	COVID-19	Viral RNA	ORF1ab, N	Yes	500 copy mL^{-1}	90 min	Shanghai GeneoDx Biotech Co., Ltd.
RT-PCR	COVID-19	Viral RNA	E, N, ORF1ab	Yes	1 copy μL^{-1}	2h	Maccura Biotechnology (USA) LLC
RT-PCR	COVID-19	Viral RNA	ORF1ab, N	Yes	200 copy mL^{-1}	90 min	Sansure BioTech Inc.
RT-LAMP[b]	COVID-19	Viral RNA	ORF1ab/E/N gene	Yes	1000 copies mL^{-1}	30 min	50
iLACO (RT-LAMP)[h]	COVID-19	Synthetic RNA	ORF1ab gene	Yes	10 copies/reaction	15–40 min	51
SHERLOCK assay (LAMP)	COVID-19	Viral RNA	N gene	Yes	100 copies/reaction	40–70 min	52
qRT-PCR (US CDC)[c]	COVID-19	Viral RNA	N1, N2, N3	Yes	1–3.2 copies μL^{-1}	>120 min	53
CRISPR/SHERLOCK[f] assay	COVID-19	Viral RNA	S,N,ORF1ab gene	Yes	42 copies μL^{-1}	>60 min	54
CRISPR-nCoV[g]	COVID-19	Viral RNA	ORF1ab gene	Yes	1.25 copies μL^{-1}	40 min	55
AIOD -CRISPR-Cas12a assay[i]	COVID-19	Viral RNA	N gene	Yes	5 copies μL^{-1}	20–40 min for extraction, 20 for reaction	56
Thermoplasmonic-Assisted Cyclic Cleavage Amplification LSPR[d]	COVID-19	Complementary DNA	ORF1ab gene	Yes	0.1 ± 0.04 pM or >10^4 copies mL^{-1}	<30 min	57
Fluorescent and colorimetric closed-tube Penn-RAMP[e]	COVID-19	Synthetic DNA	ORF1ab gene	Yes	7 copies/reaction	75 min	58
RPA/SHERLOCK[j] assay	COVID-19	Synthetic RNA	S and ORF1ab gene	Yes	10 copies μL^{-1}	1 h	59
Electrochemical DPV	COVID-19	Viral RNA	ORF1ab,N gene	No	3 aM	190 min	33
Electrochemical DPV	COVID-19	Viral RNA	S,N gene	Yes	1 copy μL^{-1}	<120 min	60
Electrochemical DPV	COVID-19	Viral RNA	ORF1ab gene	Yes	26 fM	2 h for incubating and 5 min for detection	61
Electrochemical DPV	COVID-19	Antigen	SARS-CoV-2 S-protein	No	90 fM	10–30 s	62
Electrochemical DPV	oncogenesis	Cell miRNA	microRNA-21	Yes	43.3 aM	50 min incubation time	63
Electrochemical DPV	oncogenesis	Synthetic DNA	microRNA-21	Yes	63.1 aM	9 h for incubating	64
Electrochemical DPV	oncogenesis	Synthetic DNA	microRNA-141	Yes	11 aM		65
Electrochemical open circuit voltage	oncogenesis	Synthetic DNA	microRNA-141	Yes	1.4 aM	120 min	66
current–voltage electrochemical assay	COVID-19	Viral RNA	N gene	No	6.9 copies μL^{-1}	30 min for extraction, 5 min for detection	34
Electrochemical SWV	COVID-19	Viral RNA	S and ORftab genes	No	2 and 3 copies μL^{-1}	1 h	35
Electrochemical amperometry	Cancer susceptibility and housekeeping	Synthetic DNA	TP53 and GAPDH	No	50 aM	30 min for incubating	67
Chronoamperometry	Ebola	Viral nucleic acid	EBOV cDNA	Yes	100 fM	7.5 min for incubating 1 min for detection	68
Chronoamperometry	Zika	Viral nucleic acid	ZIKV and DENV	Yes	0.7 pM		69
MECS modified graphene microelectrode using SWV and DPV	COVID-19	Viral RNA	ORF1ab gene	No	0.025 copies μL^{-1} SWV, 0.035 copies μL^{-1} DPV	30 min for incubating <1 min for detection	This work

Table 1. continued

[a]RT-PCR: Reverse Transcription-Polymerase Chain Reaction. [b]RT-LAMP: Reverse Transcription Loop-Mediated Isothermal Amplification. [c]qRT-PCR: Quantitative Reverse Transcription-Polymerase Chain Reaction. [d]LSPR: Localized Surface Plasmon Resonance. [e]Penn-RAMP: Recombinase Polymerase Amplification (RPA) (38 °C) and LAMP (63 °C). [f]CRISPR/SHERLOCK: Clustered Regularly Interspaced Short Palindromic Repeats/Specific High Sensitivity Enzymatic Reporter UnLOCKing. [g]CRISPR-nCoV: Clustered Regularly Interspaced Short Palindromic Repeats-nCoV. [h]iLACO (RT-LAMP): isothermal LAMP-based method for COVID-19. [i]RPA/SHERLOCK assay: Recombinase Polymerase Amplification/SHERLOCK assay.

(Angstrom Engineering, Canada). Afterward, the wafer was put into the Remover PG stripper solution to wipe off the photoresist. Finally, the graphene was patterned to ensure the sensing area covered the working electrodes. The electrode was treated by oxygen plasma to remove redundant graphene on the nonsensing area.

Graphene was grown by chemical vapor deposition according to reported literature.[74] First, Cu foil (25 μm) was placed in the tube furnace (GSL 1200×), and then it was heated to 1030 °C under H_2 (10 sccm, 99.999%) for 30 min. Then the Cu foil was annealed at 1030 °C in H_2 (7 sccm, 99.999%) in next 30 min. After that, CH_4 (16 sccm, 99.999%) was used for the grown process of graphene lasted for 20 min in the atmosphere of H_2 (7 sccm, 99.999%). Finally, the tube furnace was rapidly cooled to room temperature under the atmosphere of H_2. The graphene film on the Cu foil was stored under indoor temperature and dry.[75]

The MECS included an upstanding regular tetrahedral base and bioinspired tentacles. The regular tetrahedral base was a tetrahedral structure with four double-stranded DNA (Table S1). The vertex of the tentacles was modified with methylene blue as the label to generate an electrochemical response. All the DNA were prepared and purified by Sangon Biotechnology Inc. Equimolar quantities (1 μM) of four strands for the assemblage of the MECS were mixed in 1 × TM buffer at 95 °C for 10 min, and then were cooled to 4 °C immediately using a thermal cycler (SimpliAmp, Thermo Fisher Scientific).

The device was immersed in an acetone solution of 5 mM PASE for 2 h at room temperature, then washed with acetone, ethanol, and DI water three times in a turn, and dried with nitrogen in the air ambient. MECS (1 μM, 50 μL) was added to the PDMS chamber for 12 h at room temperature. After these steps, MECS was immobilized onto the graphene electrochemical microelectrodes successfully.

Characterization of MECS-Modified Graphene Microelectrodes. The morphologies of the MECS on graphene microelectrode in fluids (1 × TM) was measured by AFM (Fastscan, Bruke). As for the height variation between the bare graphene and after treatment with PASE, we took the AFM measurement operated in ScanAsyst mode using a 20−25 nm radius tip (Scanasyst air) in the air to analyze the height difference among the measured results. After being treated by PASE, the graphene was measured by a Raman spectrometer (LabRam HR Evolution, Horiba Jobin Yvon, 532 nm Ar ion laser) with the point and the mapping measurement. The fluorescence intensities were imaged using a confocal fluorescence microscope (C2+, Nikon) and measured before and after 100 μL SARS-CoV-2 IVT RNA (10^8 copies μL^{-1}) was added. XPS (Thermo Scientific K-Alpha) was used to study the modification of electrodes. COMSOL Multiphysics performed simulations of electric field distribution. The primary and secondary current distribution module simulated the electric field distribution when voltages of −0.3, −0.35, and −0.4 V were applied at the working electrode, respectively.

Preparation of Standard Samples and Clinical Samples. The samples of SARS-CoV-2, SARS-CoV, MERS-CoV IVT RNA, and human ssDNA (nt 13321−15540, GenBank Nos. MT027064.1, NC004718.3, and NC019843.3) with a titer of 10^8 copies μL^{-1} were provided by Shanghai Institute of Measurement and Testing Technology (SIMT). The samples were centrifuged at 3000 rpm at 4 °C for 5 min and diluted into 10000 copies μL^{-1} first in full artificial saliva (Solarbio, China) and 2% of RNase inhibitor

(Thermo Fisher) and then were serially diluted in full artificial saliva to concentrations of 1000, 100, 10, 1, and 0.1 copies μL^{-1}.

The clinical samples used in this study were obtained from the Department of Laboratory Medicine, Shanghai Public Health Clinical Center. Seven nasopharyngeal swab samples were from RT-PCR-positive COVID-19 patients. Seven nasopharyngeal swab samples were from healthy volunteers. Viral transport medium (500 μL, Yocon, China) was used to store the swab and was heated at 56 °C for 30 min to release the RNA. Then the 14 clinical samples were randomly divided into 42 equal-volume samples (100 μL) titled S1–S42 for double-blind testing by other experimenters who do not perform electrochemical detection of SARS-CoV-2 RNA. The mediums were directly used for SARS-CoV-2 RNA testing by MECS-modified graphene microelectrodes, without the requirement of the extraction procedure. This research was approved by the Shanghai Public Health Clinical Center Ethics Committee (approval ID No. 2020-Y114-01) with informed consent from participants.

Electrochemical Measurement. Buffer as the blank sample (80 μL) was added into the PDMS chamber for electrochemical detection. Then, 40 μL of buffer in the PDMS chamber was taken out, and 40 μL RNA samples were added. Each sample of different concentrations was measured after 30 min of incubation. An Ag/AgCl electrode was used as the reference electrode in the solution. For human ssDNA, SARS-CoV-2 IVT RNA, SARS-CoV IVT RNA, and MERS-CoV IVT RNA detection, SWV (max initial potential −0.1 V, max final potential −0.8 V, pulse height 50 mV, step height 5 mV, frequency 10 Hz) and DPV (max initial potential −0.2 V, max final potential −0.8 V, pulse height 50 mV, step height 5 mV) were performed in the as prepared solution by electrochemical workstation (CHI660e, CH Instruments Ins., Shanghai). The concentration of MERS IVT RNA, SARS-CoV IVT RNA, human IVT ssDNA are 5 copies μL^{-1}, while the concentration of SARS-CoV-2 IVT RNA is just 0.5 copies μL^{-1}.

Buffer as the blank sample (80 μL) was added into the PDMS chamber for electrochemical detection. Then 40 μL of buffer in the PDMS chamber was taken out, and 40 μL of blank samples were added again. During this process, the SWV and DPV results of the sensor signal can be used to show the stability of the baseline. After this, 40 μL of solution was taken out, and 40 μL of SARS-CoV-2 RNA samples were added into the PDMS chamber for electrochemical detection after 30 min of incubation time. Finally, the electrochemical detections were performed again after the next 30 min. The process was used to make sure the response is a result of the SARS-CoV-2 RNA.

Construction of the Electrochemical Portable Prototype. The electrochemical portable prototype was divided into the microcontroller unit (MCU, C8051, Silicon laboratories), the digital analog converter (DAC, DAC8552, TI, USA), the potentiostat (AD8606, ADI), the power management chip (TPS61085 and TPS79933), and the Bluetooth (HC-06). The prototype was programmed by KEIL. The application (APP) installed in the smartphone connected to the prototype by Bluetooth and sent commands to it. The APP was programmed by Android Studio and featured some functions including communication, data processing, data filtering, and real-time plotting.

■ ASSOCIATED CONTENT

Ⓢ Supporting Information

The Supporting Information is available free of charge at https://pubs.acs.org/doi/10.1021/jacs.2c02884.

> Calculation equation of edge effect, figures of Raman observation of graphene, graphene modified with MECS, and AFM observation of graphene, and graphene modified with MECS added SARS-CoV-2 IVT RNA (PDF)

■ AUTHOR INFORMATION

Corresponding Author

Dacheng Wei − *State Key Laboratory of Molecular Engineering of Polymers, Department of Macromolecular Science and Laboratory of Molecular Materials and Devices, Fudan University, Shanghai 200433, China;* ⓞ orcid.org/0000-0003-3593-9897; Email: weidc@fudan.edu.cn

Authors

Daizong Ji − *State Key Laboratory of Molecular Engineering of Polymers, Department of Macromolecular Science and Laboratory of Molecular Materials and Devices, Fudan University, Shanghai 200433, China*

Mingquan Guo − *Shanghai Public Health Clinical Center, Fudan University, Shanghai 201508, China*

Yungen Wu − *State Key Laboratory of Molecular Engineering of Polymers, Department of Macromolecular Science and Laboratory of Molecular Materials and Devices, Fudan University, Shanghai 200433, China*

Wentao Liu − *State Key Laboratory of Molecular Engineering of Polymers, Department of Macromolecular Science and Laboratory of Molecular Materials and Devices, Fudan University, Shanghai 200433, China*

Shi Luo − *State Key Laboratory of Molecular Engineering of Polymers, Department of Macromolecular Science and Laboratory of Molecular Materials and Devices, Fudan University, Shanghai 200433, China*

Xuejun Wang − *State Key Laboratory of Molecular Engineering of Polymers, Department of Macromolecular Science and Laboratory of Molecular Materials and Devices, Fudan University, Shanghai 200433, China;* ⓞ orcid.org/0000-0002-7034-0460

Hua Kang − *State Key Laboratory of Molecular Engineering of Polymers, Department of Macromolecular Science and Laboratory of Molecular Materials and Devices, Fudan University, Shanghai 200433, China*

Yiheng Chen − *State Key Laboratory of Molecular Engineering of Polymers, Department of Macromolecular Science and Laboratory of Molecular Materials and Devices, Fudan University, Shanghai 200433, China*

Changhao Dai − *State Key Laboratory of Molecular Engineering of Polymers, Department of Macromolecular Science and Laboratory of Molecular Materials and Devices, Fudan University, Shanghai 200433, China;* ⓞ orcid.org/0000-0002-0696-077X

Derong Kong − *State Key Laboratory of Molecular Engineering of Polymers, Department of Macromolecular Science and Laboratory of Molecular Materials and Devices, Fudan University, Shanghai 200433, China*

Hongwenjie Ma − *State Key Laboratory of Molecular Engineering of Polymers, Department of Macromolecular*

Science and Laboratory of Molecular Materials and Devices, Fudan University, Shanghai 200433, China

Yunqi Liu − Laboratory of Molecular Materials and Devices, Fudan University, Shanghai 200433, China; Institute of Chemistry, Chinese Academy of Science, Beijing 100190, China; ⊙ orcid.org/0000-0001-5521-2316

Complete contact information is available at:
https://pubs.acs.org/10.1021/jacs.2c02884

Author Contributions

The manuscript was written through contributions of all authors. All authors have given approval to the final version of the manuscript.

Notes

The authors declare no competing financial interest.

ACKNOWLEDGMENTS

REFERENCES

(1) WHO. Coronavirus Disease (COVID-19) Dashboard. https://covid19.who.int (accessed 2022-05-06).

(2) WHO. Classification of Omicron (B.1.1.529): SARS-CoV-2 Variant of Concern. https://www.who.int/news/item/26-11-2021-classification-of-omicron-(b.1.1.529)-sars-cov-2-variant-of-concern (accessed 2022-01-25).

(3) Chookajorn, T.; Kochakarn, T.; Wilasang, C.; Kotanan, N.; Modchang, C. Southeast Asia is an emerging hotspot for COVID-19. Nat. Med. 2021, 27, 1495−1496.

(4) Cevik, M.; Grubaugh, N. D.; Iwasaki, A.; Openshaw, P. COVID-19 vaccines: Keeping pace with SARS-CoV-2 variants. Cell 2021, 184, 5077−5081.

(5) Faria, H. A. M.; Zucolotto, V. Label-free electrochemical DNA biosensor for zika virus identification. Biosens. Bioelectron 2019, 131, 149−155.

(6) Musso, D.; Roche, C.; Nhan, T.-X.; Robin, E.; Teissier, A.; Cao-Lormeau, V.-M. Detection of Zika virus in saliva. J. Clin. Virol 2015, 68, 53−55.

(7) Qin, P.; Park, M.; Alfson, K. J.; Tamhankar, M.; Carrion, R.; Patterson, J. L.; Griffiths, A.; He, Q.; Yildiz, A.; Mathies, R. Rapid and fully microfluidic Ebola virus detection with CRISPR-Cas13a. ACS Sensors 2019, 4, 1048−1054.

(8) Seo, G.; Lee, G.; Kim, M. J.; Baek, S.-H.; Choi, M.; Ku, K. B.; Lee, C.-S.; Jun, S.; Park, D.; Kim, H. G. Rapid detection of COVID-19 causative virus (SARS-CoV-2) in human nasopharyngeal swab specimens using field-effect transistor-based biosensor. ACS Nano 2020, 14, 5135−5142.

(9) Waller, J. V.; Kaur, P.; Tucker, A.; Lin, K. K.; Diaz, M. J.; Henry, T. S.; Hope, M. Diagnostic tools for coronavirus disease (COVID-19): comparing CT and RT-PCR viral nucleic acid testing. Am. J. Roentgenol 2020, 215, 834−838.

(10) Broughton, J. P.; Deng, X.; Yu, G.; Fasching, C. L.; Servellita, V.; Singh, J.; Miao, X.; Streithorst, J. A.; Granados, A.; Sotomayor-Gonzalez, A. CRISPR−Cas12-based detection of SARS-CoV-2. Nat. Biotechnol. 2020, 38, 870−874.

(11) Chan, J. F.-W.; Yip, C. C.-Y.; To, K. K.-W.; Tang, T. H.-C.; Wong, S. C.-Y.; Leung, K.-H.; Fung, A. Y.-F.; Ng, A. C.-K.; Zou, Z.; Tsoi, H.-W. Improved molecular diagnosis of COVID-19 by the novel, highly sensitive and specific COVID-19-RdRp/Hel real-time reverse transcription-PCR assay validated in vitro and with clinical specimens. J. Clin. Microbiol 2020, 58, No. e00310.

(12) Asif, M.; Ajmal, M.; Ashraf, G.; Muhammad, N.; Aziz, A.; Iftikhar, T.; Wang, J.; Liu, H. The role of biosensors in COVID-19 outbreak. Curr. Opin. Electroche 2020, 23, 174−184.

(13) Hwang, M. T.; Heiranian, M.; Kim, Y.; You, S.; Leem, J.; Taqieddin, A.; Faramarzi, V.; Jing, Y.; Park, I.; Van Der Zande, A. M. Ultrasensitive detection of nucleic acids using deformed graphene channel field effect biosensors. Nat. Commun. 2020, 11, 1543.

(14) Pokhrel, P.; Hu, C.; Mao, H. Detecting the coronavirus (COVID-19). ACS Sensors 2020, 5, 2283−2296.

(15) Hassan, S. A.; Sheikh, F. N.; Jamal, S.; Ezeh, J. K.; Akhtar, A. Coronavirus (COVID-19): a review of clinical features, diagnosis, and treatment. Cureus 2020, 12, No. e7355.

(16) Ning, B.; Yu, T.; Zhang, S.; Huang, Z.; Tian, D.; Lin, Z.; Niu, A.; Golden, N.; Hensley, K.; Threeton, B.; Lyon, C. J.; Yin, X.-M.; Roy, C. J.; Saba, N. S.; Rappaport, J.; Wei, Q.; Hu, T. Y. A smartphone-read ultrasensitive and quantitative saliva test for COVID-19. Sci. Adv. 2021, 7, No. eabe3703.

(17) Wang, L.; Wang, X.; Wu, Y.; Guo, M.; Gu, C.; Dai, C.; Kong, D.; Wang, Y.; Zhang, C.; Qu, D.; Fan, C.; Xie, Y.; Zhu, Z.; Liu, Y.; Wei, D. Rapid and ultrasensitive electromechanical detection of ions, biomolecules and SARS-CoV-2 RNA in unamplified samples. Nat. Biomed. Eng. 2022, 6, 276−285.

(18) Wang, X.; Kong, D.; Guo, M.; Wang, L.; Gu, C.; Dai, C.; Wang, Y.; Jiang, Q.; Ai, Z.; Zhang, C.; Qu, D.; Xie, Y.; Zhu, Z.; Liu, Y.; Wei, D. Rapid SARS-CoV-2 Nucleic Acid Testing and Pooled Assay by Tetrahedral DNA Nanostructure Transistor. Nano Lett. 2021, 21, 9450−9457.

(19) Norton, J. D.; White, H. S.; Feldberg, S. W. Effect of the electrical double layer on voltammetry at microelectrodes. J. Phys. Chem. 1990, 94, 6772−6780.

(20) Forster, R. J. Microelectrodes: new dimensions in electro-chemistry. Chem. Soc. Rev. 1994, 23, 289−297.

(21) da Silva, E. T.; Souto, D. E.; Barragan, J. T.; de F. Giarola, J.; de Moraes, A. C.; Kubota, L. T. Electrochemical biosensors in point-of-care devices: recent advances and future trends. ChemElectroChem. 2017, 4, 778−794.

(22) Shin Low, S.; Pan, Y.; Ji, D.; Li, Y.; Lu, Y.; He, Y.; Chen, Q.; Liu, Q. Smartphone-based portable electrochemical biosensing system for detection of circulating microRNA-21 in saliva as a proof-of-concept. Sensor. Actuat. B-Chem. 2020, 308, 127718.

(23) Shuai, H.-L.; Huang, K.-J.; Xing, L.-L.; Chen, Y.-X. Ultra-sensitive electrochemical sensing platform for microRNA based on tungsten oxide-graphene composites coupling with catalyzed hairpin assembly target recycling and enzyme signal amplification. Biosens. Bioelectron 2016, 86, 337−345.

(24) Wu, Y.; Tilley, R. D.; Gooding, J. J. Challenges and solutions in developing ultrasensitive biosensors. J. Am. Chem. Soc. 2019, 141, 1162−1170.

(25) Kudr, J.; Michalek, P.; Ilieva, L.; Adam, V.; Zitka, O. COVID-19: A challenge for electrochemical biosensors. TrAC Trends Anal. Chem. 2021, 136, 116192.

(26) Campuzano, S.; Pedrero, M.; Pingarrón, J. M. Electrochemical genosensors for the detection of cancer-related miRNAs. Anal. Bioanal. Chem. 2014, 406, 27−33.

(27) Santhanam, M.; Algov, I.; Alfonta, L. DNA/RNA electro-chemical biosensing devices a future replacement of PCR methods for a fast epidemic containment. Sensors 2020, 20, 4648.

(28) Kesler, V.; Murmann, B.; Soh, H. T. Going beyond the debye length: Overcoming charge screening limitations in next-generation bioelectronic sensors. ACS Nano 2020, 14, 16194−16201.

(29) Islam, M. N.; Masud, M. K.; Haque, M. H.; Hossain, M. S. A.; Yamauchi, Y.; Nguyen, N. T.; Shiddiky, M. J. RNA biomarkers:

diagnostic and prognostic potentials and recent developments of electrochemical biosensors. *Small Methods* **2017**, *1*, 1700131.

(30) Brazaca, L. C.; Dos Santos, P. L.; de Oliveira, P. R.; Rocha, D. P.; Stefano, J. S.; Kalinke, C.; Muñoz, R. A. A.; Bonacin, J. A.; Janegitz, B. C.; Carrilho, E. Biosensing strategies for the electrochemical detection of viruses and viral diseases−A review. *Anal. Chim. Acta* **2021**, *1159*, 338384.

(31) Masud, M. K.; Umer, M.; Hossain, M. S. A.; Yamauchi, Y.; Nguyen, N.-T.; Shiddiky, M. J. Nanoarchitecture frameworks for electrochemical miRNA detection. *Trends Biochem. Sci.* **2019**, *44*, 433−452.

(32) Low, S. S.; Ji, D.; Chai, W. S.; Liu, J.; Khoo, K. S.; Salmanpour, S.; Karimi, F.; Deepanraj, B.; Show, P. L. Recent Progress in Nanomaterials Modified Electrochemical Biosensors for the Detection of MicroRNA. *Micromachines* **2021**, *12*, 1409.

(33) Zhao, H.; Liu, F.; Xie, W.; Zhou, T.-C.; OuYang, J.; Jin, L.; Li, H.; Zhao, C.-Y.; Zhang, L.; Wei, J. Ultrasensitive supersandwich-type electrochemical sensor for SARS-CoV-2 from the infected COVID-19 patients using a smartphone. *Sensor Actuat. B-Chem.* **2021**, *327*, 128899.

(34) Alafeef, M.; Dighe, K.; Moitra, P.; Pan, D. Rapid, ultrasensitive, and quantitative detection of SARS-CoV-2 using antisense oligonucleotides directed electrochemical biosensor chip. *ACS Nano* **2020**, *14*, 17028−17045.

(35) Kashefi-Kheyrabadi, L.; Nguyen, H. V.; Go, A.; Baek, C.; Jang, N.; Lee, J. M.; Cho, N.-H.; Min, J.; Lee, M.-H. Rapid, multiplexed, and nucleic acid amplification-free detection of SARS-CoV-2 RNA using an electrochemical biosensor. *Biosens. Bioelectron* **2022**, *195*, 113649.

(36) Kim, J.-Y.; Yun, Y. J.; Jeong, J.; Kim, C.-Y.; Müller, K.-R.; Lee, S.-W. Leaf-inspired homeostatic cellulose biosensors. *Sci. Adv.* **2021**, *7*, No. eabe7432.

(37) Priemel, T.; Palia, G.; Förste, F.; Jehle, F.; Sviben, S.; Mantouvalou, I.; Zaslansky, P.; Bertinetti, L.; Harrington, M. J. Microfluidic-like fabrication of metal ion−cured bioadhesives by mussels. *Science* **2021**, *374*, 206−211.

(38) Connors, M.; Yang, T.; Hosny, A.; Deng, Z.; Yazdandoost, F.; Massaadi, H.; Eernisse, D.; Mirzaeifar, R.; Dean, M. N.; Weaver, J. C. Bioinspired design of flexible armor based on chiton scales. *Nat. Commun.* **2019**, *10*, 5413.

(39) Li, S.; Bai, H.; Shepherd, R. F.; Zhao, H. Bio-inspired design and additive manufacturing of soft materials, machines, robots, and haptic interfaces. *Angew. Chem. Int. Ed* **2019**, *58*, 11182−11204.

(40) Naik, R. R.; Singamaneni, S. Introduction: bioinspired and biomimetic materials. *Chem. Rev.* **2017**, *117*, 12581−12583.

(41) Yue, O.; Wang, X.; Liu, X.; Hou, M.; Zheng, M.; Wang, Y.; Cui, B. Spider-web and ant-tentacle doubly bio-inspired multifunctional self-powered electronic skin with hierarchical nanostructure. *Adv. Sci.* **2021**, *8*, 2004377.

(42) McKinney, F. K. Bryozoan-hydroid symbiosis and a new ichnogenus, Caupokeras. *Ichnos* **2009**, *16*, 193−201.

(43) Wang, H.; Su, X.; Chai, Z.; Tian, Z.; Xie, W.; Wang, Y.; Wan, Z.; Deng, M.; Yuan, Z.; Huang, J. A hydra tentacle-inspired hydrogel with underwater ultra-stretchability for adhering adipose surfaces. *Chem. Eng. J.* **2022**, *428*, 131049.

(44) Wood, R. L.; Novak, P. L. The anchoring of nematocysts and nematocytes in the tentacles of hydra. *J. Ultrastru. Res.* **1982**, *81*, 104−116.

(45) Liu, Y.; Yuan, L.; Yang, M.; Zheng, Y.; Li, L.; Gao, L.; Nerngchamnong, N.; Nai, C. T.; Sangeeth, C. S.; Feng, Y. P. Giant enhancement in vertical conductivity of stacked CVD graphene sheets by self-assembled molecular layers. *Nat. Commun.* **2014**, *5*, 5461.

(46) Liu, J.-Y.; Chang, H.-Y.; Truong, Q. D.; Ling, Y.-C. Synthesis of nitrogen-doped graphene by pyrolysis of ionic-liquid-functionalized graphene. *J. Mater. Chem. C* **2013**, *1*, 1713−1716.

(47) Wu, G.; Tang, X.; Meyyappan, M.; Lai, K. W. C. Doping effects of surface functionalization on graphene with aromatic molecule and organic solvents. *Appl. Surf. Sci.* **2017**, *425*, 713−721.

(48) Kong, D.; Wang, X.; Gu, C.; Guo, M.; Wang, Y.; Ai, Z.; Zhang, S.; Chen, Y.; Liu, W.; Wu, Y.; Dai, C.; Guo, Q.; Qu, D.; Zhu, Z.; Xie, Y.; Liu, Y.; Wei, D. Direct SARS-CoV-2 nucleic acid detection by y-shaped DNA dual-probe transistor assay. *J. Am. Chem. Soc.* **2021**, *143*, 17004−17014.

(49) Dai, C.; Guo, M.; Wu, Y.; Cao, B.-P.; Wang, X.; Wu, Y.; Kang, H.; Kong, D.; Zhu, Z.; Ying, T.; Zhu, Z.; Wei, D.; Liu, Y.; Wei, D. Ultraprecise Antigen 10-in-1 pool testing by multiantibodies transistor assay. *J. Am. Chem. Soc.* **2021**, *143*, 19794−19801.

(50) Yang, W.; Dang, X.; Wang, Q.; Xu, M.; Zhao, Q.; Zhou, Y.; Zhao, H.; Wang, L.; Xu, Y.; Wang, J., Rapid detection of SARS-CoV-2 using reverse transcription RT-LAMP method. March 3, 2020. *MedRxiv*, https://www.medrxiv.org/content/10.1101/2020.03.02. 20030130v2.full-text (accessed 2022-01-28).

(51) Yu, L.; Wu, S.; Hao, X.; Dong, X.; Mao, L.; Pelechano, V.; Chen, W.-H.; Yin, X. Rapid detection of COVID-19 coronavirus using a reverse transcriptional loop-mediated isothermal amplification (RT-LAMP) diagnostic platform. *Clin. Chem.* **2020**, *66*, 975−977.

(52) Joung, J.; Ladha, A.; Saito, M.; Segel, M.; Bruneau, R.; Huang, M.-L. W.; Kim, N.-G.; Yu, X.; Li, J.; Walker, B. D., Point-of-care testing for COVID-19 using SHERLOCK diagnostics *MedRxiv* **2020**. DOI: 10.1101/2020.05.04.20091231

(53) Centers for Disease Control and Prevention, CDC 2019-novel coronavirus (2019-nCoV) real-time RT-PCR diagnostic panel. https://www.fda.gov/media/134922/download (accessed 2022-02-08).

(54) Patchsung, M.; Jantarug, K.; Pattama, A.; Aphicho, K.; Suraritdechachai, S.; Meesawat, P.; Sappakhaw, K.; Leelahakorn, N.; Ruenkam, T.; Wongsatit, T. Clinical validation of a Cas13-based assay for the detection of SARS-CoV-2 RNA. *Nat. Biomed. Eng.* **2020**, *4*, 1140−1149.

(55) Hou, T.; Zeng, W.; Yang, M.; Chen, W.; Ren, L.; Ai, J.; Wu, J.; Liao, Y.; Gou, X.; Li, Y. Development and evaluation of a rapid CRISPR-based diagnostic for COVID-19. *PLoS Pathog* **2020**, *16*, No. e1008705.

(56) Ding, X.; Yin, K.; Li, Z.; Lalla, R. V.; Ballesteros, E.; Sfeir, M. M.; Liu, C. Ultrasensitive and visual detection of SARS-CoV-2 using all-in-one dual CRISPR-Cas12a assay. *Nat. Commun.* **2020**, *11*, 4711.

(57) Qiu, G.; Gai, Z.; Saleh, L.; Tang, J.; Gui, T.; Kullak-Ublick, G. A.; Wang, J. Thermoplasmonic-assisted cyclic cleavage amplification for self-validating plasmonic detection of SARS-CoV-2. *ACS Nano* **2021**, *15*, 7536−7546.

(58) El-Tholoth, M.; Bau, H. H.; Song, J., A single and two-stage, closed-tube, molecular test for the 2019 novel coronavirus (COVID-19) at home, clinic, and points of entry. *ChemRxiv*. February 19, **2020**. https://www.ncbi.nlm.nih.gov/pmc/articles/PMC7251958/ (accessed 2022-02-13).

(59) Zhang, F.; Abudayyeh, O. O.; Gootenberg, J. S., A protocol for detection of COVID-19 using CRISPR diagnostics. https://broad.io/ sherlockprotocol. (accessed 2022-02-08).

(60) Chaibun, T.; Puenpa, J.; Ngamdee, T.; Boonapatcharoen, N.; Athamanolap, P.; O'Mullane, A. P.; Vongpunsawad, S.; Poovorawan, Y.; Lee, S. Y.; Lertanantawong, B. Rapid electrochemical detection of coronavirus SARS-CoV-2. *Nat. Commun.* **2021**, *12*, 802.

(61) Peng, Y.; Pan, Y.; Sun, Z.; Li, J.; Yi, Y.; Yang, J.; Li, G. An electrochemical biosensor for sensitive analysis of the SARS-CoV-2 RNA. *Biosens. Bioelectron* **2021**, *186*, 113309.

(62) Mahari, S.; Roberts, A.; Shahdeo, D.; Gandhi, S., eCovSens-ultrasensitive novel in-house built printed circuit board based electrochemical device for rapid detection of nCovid-19 antigen, a spike protein domain 1 of SARS-CoV-2. *BioRxiv* May 11, **2020**. URL: https://www.biorxiv.org/content/10.1101/2020.04.24.059204v3.full (accessed 2022-02-03).

(63) Zhang, H.; Fan, M.; Jiang, J.; Shen, Q.; Cai, C.; Shen, J. Sensitive electrochemical biosensor for MicroRNAs based on duplex-specific nuclease-assisted target recycling followed with gold nanoparticles and enzymatic signal amplification. *Anal. Chim. Acta* **2019**, *1064*, 33−39.

(64) Meng, T.; Jia, H.; An, S.; Wang, H.; Yang, X.; Zhang, Y. Pd nanoparticles-DNA layered nanoreticulation biosensor based on target-catalytic hairpin assembly for ultrasensitive and selective biosensing of microRNA-21. *Sensor. Actuat. B-Chem.* **2020**, *323*, 128621.

(65) Yuan, Y.-H.; Chi, B.-Z.; Wen, S.-H.; Liang, R.-P.; Li, Z.-M.; Qiu, J.-D. Ratiometric electrochemical assay for sensitive detecting microRNA based on dual-amplification mechanism of duplex-specific nuclease and hybridization chain reaction. *Biosens. Bioelectron* **2018**, *102*, 211−216.

(66) Zhang, T.; Chai, H.; Meng, F.; Guo, Z.; Jiang, Y.; Miao, P. DNA-functionalized porous Fe_3O_4 nanoparticles for the construction of self-powered miRNA biosensor with target recycling amplification. *ACS Appl. Mater. Inter* **2018**, *10*, 36796−36804.

(67) Xie, H.; Yu, Y. H.; Xie, F.; Lao, Y. Z.; Gao, Z. A nucleic acid biosensor for gene expression analysis in nanograms of mRNA. *Anal. Chem.* **2004**, *76*, 4023−4029.

(68) Ciftci, S.; Cánovas, R.; Neumann, F.; Paulraj, T.; Nilsson, M.; Crespo, G. A.; Madaboosi, N. The sweet detection of rolling circle amplification: Glucose-based electrochemical genosensor for the detection of viral nucleic acid. *Biosens. Bioelectron* **2020**, *151*, 112002.

(69) Alzate, D.; Cajigas, S.; Robledo, S.; Muskus, C.; Orozco, J. Genosensors for differential detection of Zika virus. *Talanta* **2020**, *210*, 120648.

(70) Peeling, R. W.; Olliaro, P. L.; Boeras, D. I.; Fongwen, N. Scaling up COVID-19 rapid antigen tests: promises and challenges. *Lancet Infect. Dis* **2021**, *21*, No. e290.

(71) Green, K.; Winter, A.; Dickinson, R.; Graziadio, S.; Wolff, R.; Mallett, S.; Allen, A. J.; Park, E. What tests could potentially be used for the screening, diagnosis and monitoring of COVID-19 and what are their advantages and disadvantages *CEBM2020* **2020**, *13*.

(72) Service, R. F. Fast, cheap tests could enable safer reopening. *Science* **2020**, *369*, 608−609.

(73) Wang, X.; Hao, Z.; Olsen, T. R.; Zhang, W.; Lin, Q. Measurements of aptamer−protein binding kinetics using graphene field-effect transistors. *Nanoscale* **2019**, *11*, 12573−12581.

(74) Li, X.; Cai, W.; An, J.; Kim, S.; Nah, J.; Yang, D.; Piner, R.; Velamakanni, A.; Jung, I.; Tutuc, E. Large-area synthesis of high-quality and uniform graphene films on copper foils. *Science* **2009**, *324*, 1312−1314.

(75) Gao, L.; Ren, W.; Xu, H.; Jin, L.; Wang, Z.; Ma, T.; Ma, L.-P.; Zhang, Z.; Fu, Q.; Peng, L.-M. Repeated growth and bubbling transfer of graphene with millimetre-size single-crystal grains using platinum. *Nat. Commun.* **2012**, *3*, 699.